Chemical Engineering Journal 548 (2026) 181531

Contents lists available at ScienceDirect

Chemical Engineering Journal

journal homepage: www.elsevier.com/locate/cej

Geometry-driven negative Poisson's ratio yarns for anisotropic strain sensing

Guicen Liu [a], Long Jin [a,*], Yong Ao [a], Boling Lan [a], Tianpei Xu [a], Shenglong Wang [a], Tingting Zhou [a], Zihan Wang [a], Wei Zhao [a], Zhiyuan Gao [a], Weili Deng [a], Weiqing Yang [a,b]

[a] Key Laboratory of Advanced Technologies of Materials (Ministry of Education), School of Materials Science and Engineering, Southwest Jiaotong University, Chengdu, 610031, PR China

[b] Research Institute of Frontier Science, Southwest Jiaotong University, Chengdu, Sichuan, 610031, PR China

ARTICLE INFO

Keywords:
Negative Poisson's ratio structure
Piezoelectric sensors
Anisotropic strain sensing
PVDF-TrFE

ABSTRACT

Yarn-based sensors offer excellent conformability for wearable electronics on complex body surfaces. Yet existing sensing mechanisms face a fundamental limitation: interface-dominated approaches suffer from signal stochasticity and drift due to contact interface instability, while piezoelectric alternatives remain restricted to uniaxial responses incapable of discriminating coupled multi-axial deformations. Here, a geometry-engineered negative Poisson's ratio piezoelectric yarn sensor is designed to integrate geometry-driven deformation with strain-induced piezoelectric polarization. The helical scaffold transforms axial stretching into radial expansion through structural rearrangement, which enables a single mechanical stimulus to generate distinguishable electrical responses along different axes. Upon axial stretching, the helical windings undergo coordinated rearrangement that converts the longitudinal extension into pronounced radial expansion, intrinsically coupling the longitudinal and transverse deformation pathways within the same fiber architecture. This geometry-driven strain redistribution yields a piezoelectric output of 5.10 V under 30% tensile strain, representing a 42-fold enhancement over conventional positive Poisson's ratio yarns, with stable operation over 10,000 cycles. The resulting demonstrates effective monitoring of multi-axial deformations, including axial stretching, normal pressure, and bending gradients. As a proof of concept, the sensor enables closed-loop rehabilitation training feedback, establishing a geometry-driven strategy for wearable anisotropic biomechanical monitoring on complex body surfaces.

1. Introduction

Driven by the rapid advancement of wearable medical electronics and rehabilitation monitoring systems, the demand for continuous and reliable biomechanical monitoring has grown significantly [1–4]. Flexible strain sensors have attracted extensive attention due to their intrinsic flexibility, stretchability, and lightweight characteristics [5–9]. They exhibit advantages in large strain range and high sensitivity aspects [10–12], achieving precise conformability on complex curved surfaces remains challenging, primarily due to insufficient structural compliance [13–16]. To address this issue, integrating sensors with textiles has emerged as an effective strategy for wearable sensing applications [17–20]. Compared with a two-dimensional fabric-based strain sensor [18], a one-dimensional fabric-based strain sensor enables efficient axial deformation transmission, minimizes interfacial slip, and yield stable electromechanical effect responses by integrating structural support and sensing functionality within a unified one-dimensional fiber architecture [21,22]. The confined axial deformation pathway further enhances directional electromechanical effect coupling and mechanical-to-electrical conversion efficiency [23,24]. These attributes position, yarn-based strain sensors as a highly promising platform for long-term human motion monitoring.

High-performance yarn-based strain sensors typically rely on structural design strategies to simultaneously achieve superior sensing performance and seamless integration within textiles. At present, most yarn strain sensors adopt configurations such as uniform coating structures [25], core–sheath structures, crack-engineered structures, braided structures [26–31]. They predominantly rely on interfacial variations for signal generation, whereas the dynamically non-uniform nature of interface-dominated mechanisms inherently induces signal

* Corresponding author.
E-mail address: longjin@swjtu.edu.cn (L. Jin).

https://doi.org/10.1016/j.cej.2026.181531
Received 13 July 2026; Received in revised form 16 August 2026; Accepted 2 September 2026
Available online 17 September 2026
1385-8947/© 2026 Elsevier B.V. All rights are reserved, including those for text and data mining, AI training, and similar technologies.

stochasticity, hysteresis, and drift, thereby limiting sensing reliability under repeated cycling [32–35]. In contrast, strain-induced polarization in piezoelectric polymers enables physically correlated, direction-sensitive electromechanical effect transduction without reliance on unstable interfacial states [36,37]. The intrinsic responsiveness is particularly compatible with geometry-engineered deformation systems, where structural topology rather than surface state dictates the strain distribution. However, uniaxial piezoelectric coupling alone is inherently insufficient for resolving complex multidirectional mechanical stimuli, as human motion inherently involves coupled multi-axial deformations, including spanning axial stretching, normal pressure, and bending gradients [38]. Discriminating these distinct mechanical stimuli from a single sensing element therefore requires anisotropic transduction capabilities [39]. Conventional anisotropic force sensing systems predominantly depend on structurally partitioned architectures or sensor arrays, where multidirectional force information is reconstructed from coupled electrical outputs through calibration or data-driven decoupling [40,41]. Such post-processed sensing paradigms inherently suffer from mechanical crosstalk and limited stability under complex deformation conditions [42]. To overcome the limitations, a one-dimensional piezoelectric sensing mechanism featuring geometry-driven intrinsic strain response is required to achieve stable anisotropic transduction in a unified fiber architecture.

Here, we report a flexible geometry-driven negative Poisson's ratio (NPR) piezoelectric yarn sensor (NPYS) that embeds intrinsic anisotropic strain sensing within a single fiber architecture [43,44]. The

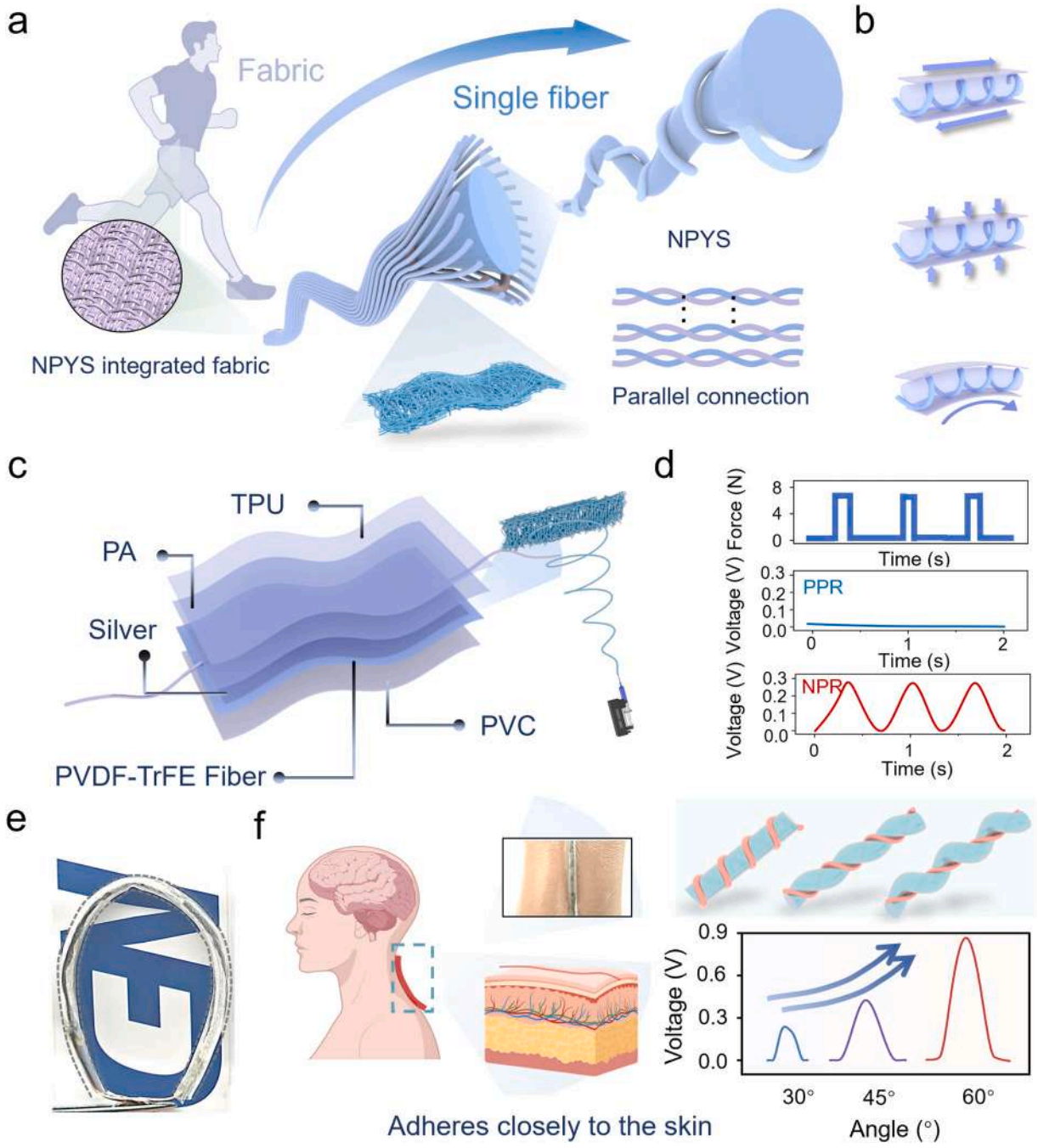


Fig. 1. NPYS Overview. a) Schematic illustration of the fabrication process of NPYS from an integrated textile to an individual yarn. b) Three representative operation modes of NPYS. c) Structural schematic of NPYS. d) Comparison of voltage outputs between PPR and NPR yarn sensors under identical loading conditions. e) Physical image of NPYS. f) S Schematic illustration of NPYS applied for monitoring neck bending angle.

geometry-driven principle refers to a deformation mechanism governed by the topological architecture of the helical NPR structure. Specifically, the design leverages an NPR scaffold in which the helical topology directs deformation pathways and redistributes axial strain into radial expansion, thereby establishing intrinsic coupling between longitudinal and transverse deformations [45]. This geometry-induced strain redistribution enables the same mechanical stimulus to generate distinguishable electrical responses along different axes, achieving direction-dependent piezoelectric transduction without structural partitioning or post-processing. Finite element simulations and experimental results elucidate the electromechanical effect of NPYS under tensile and compressive deformations, as well as the effects of structural parameters on the NPR structure characteristics and piezoelectric performance. The resulting sensor demonstrates stable, intrinsic anisotropic sensing across multiple deformation modes. As a proof of concept, an NPYS-based rehabilitation training monitoring system is developed to enable real-time tracking of human motion and feedback on movement accuracy. This work establishes a geometry-driven strategy for anisotropic piezoelectric yarn sensors and provides a viable pathway toward self-powered electronic textile systems.

2. Results and discussions

2.1. Design and preparation of NPYS

Achieving anisotropic piezoelectric sensing within a single structure requires direction-dependent deformation and stress-transfer pathways that enable distinct electrical responses under different mechanical stimuli. The NPR architecture provides an effective strategy by introducing geometry-driven structural reconfiguration. In NPYS, the helical PA/TPU scaffold undergoes unfolding and reconstruction under axial stretching, resulting in coupled axial elongation and radial expansion, which is a characteristic deformation of NPR structures (Fig. S3). This unique behavior enables NPYS to respond differently to axial stretching, transverse compression, and bending deformation (Fig. 1b). Specifically, Under transverse compression, the external force is primarily applied in the radial direction, resulting in radial compression of the piezoelectric layer. In contrast, during bending deformation, normal loading generates a strain gradient through the thickness of the device, causing the PVDF-TrFE layer to experience bending-induced stress. Therefore, the NPR architecture regulates deformation modes and stress distributions under different loading directions, enabling anisotropic piezoelectric sensing. Based on this design principle, Fig. 1a illustrates the fabrication process of NPYS from individual yarns to textile integration. A flexible yet non-elastic polyamide (PA) yarn is first helically wound around an elastic thermoplastic polyurethane (TPU) core to construct the NPR functional scaffold. Subsequently, an electrospun PVDF-TrFE nanofiber film is wrapped around the scaffold as the piezoelectric sensing layer, followed by PVC heat sealing to achieve stable encapsulation and conformal interfacial contact. The cross-sectional structure of NPYS is presented in Fig. S1, while parallel stitching of individual yarns enables textile-level integration (Fig. S2). The internal multilayer configuration and interfacial arrangement are further revealed through the side-cut cross-sectional view (Fig. 1c).

To elucidate whether the piezoelectric response of NPYS is primarily associated with the NPR effect,

NPYS and PPYS were fabricated using the same PA sheath yarn, TPU elastic core yarn, and identical PVDF-TrFE piezoelectric film, and subsequently tested under identical mechanical loading and electrical measurement conditions. In contrast to the negligible response observed in the PPR yarn, NPYS exhibits stable and reproducible piezoelectric signals (Fig. 1d). Consistently, Fig. S4 shows that, although NPYS and PPYS were fabricated using the same PA sheath yarn, TPU core yarn, and PVDF-TrFE piezoelectric film, PPYS exhibits lateral contraction under axial stretching, whereas NPYS displays pronounced lateral expansion under the same deformation; The yarn diameter was determined from the global outer envelope contour and averaged over multiple measurements to minimize the influence of local PA fiber texture on the calculated Poisson's ratio. These results further confirm the critical role of the NPR structure in activating the piezoelectric effect. Fig. 1e presents an image of NPYS under bending deformation. As a proof of concept, NPYS was attached to the posterior neck region of a human subject to monitor head-down motions and their amplitudes. The results demonstrate clear correlations between the deformation behavior of the yarn structure and the corresponding electrical signal variations during motion (Fig. 1f). Based on this capability, a rehabilitation training system was further developed for systematic human motion monitoring.

2.2. Characterization of NPR and mechanical properties of NPYS

The deformation behavior under tensile loading is first examined using a simplified model of a single-strand helically wound yarn with an NPR structure. As illustrated in Figs. 2a and S5, the axial and radial deformation of the helical structure during stretching is schematically depicted. With increasing tensile strain, the radial cross-sectional area initially decreases and subsequently increases. This nonmonotonic behavior arises from the residual torque between the sheath and the core yarn in the absence of external constraints [38]. At low tensile strains (0–10%), the system tends toward force and torque equilibrium, leading the sheath yarn to tighten around the core and causing radial contraction, corresponding to an apparent PPR [36]. Upon further elongation, the mismatch in elastic moduli between the two yarns induces straightening of the sheath yarn accompanied by bending of the core yarn. This structural rearrangement results in a configuration in which the core yarn helically wraps around the sheath, giving rise to a pronounced NPR. Here, the Poisson's ratio (ν) is defined as the ratio of transverse strain perpendicular to the loading direction to the applied longitudinal tensile strain.

$$\nu = -\varepsilon_x/\varepsilon_y \tag{2-1}$$

$$\varepsilon_x = (d_1 - d_0)/d_0 \tag{2-2}$$

$$\varepsilon_y = (l_1 - l_0)/l_0 \tag{2-3}$$

Here, ε_x and ε_y denote the radial and axial strains of NPYS, respectively. The reported Poisson's ratio represents a structural (effective) Poisson's ratio determined from the global yarn deformation. d_0 and d_1 represent the yarn diameter before and after stretching, while l_0 and l_1 denote the device length before and after deformation. The evolution of cross-sectional area and diameter during tensile deformation is shown in Fig. 2b. The corresponding Poisson's ratio calculated from the above relation is plotted in Fig. 2c, in good agreement with the preceding analysis. For clarity, the piezoelectric yarn sensor with a PPR is hereafter referred to as PPYS. To further verify that this behavior originates exclusively from the helical NPR structure, the radial diameter variations of NPYS and PPYS were quantitatively compared under identical tensile strain levels (Fig. 2d). The results show that PPYS exhibits continuous radial contraction with increasing axial strain, characteristic of a PPR, whereas NPYS displays a distinct tensile-induced radial expansion. These results confirm that the helical architecture endows the yarn with a unique tensile–expansion deformation mode.

As shown in Fig. 2e, under identical tensile strain, the single-turn helical pitch (P) markedly influences the Poisson's ratio of the structure. The fitted results indicate that an NPR emerges only when P exceeds 4.86 mm. This behavior originates from the critical role of pitch in governing the deformation pathway of the helical geometry. At small pitches, geometric reconstruction of the helix is suppressed under low axial strain, thereby inhibiting the onset of NPR behavior. When P surpasses a threshold value, relative positional deflection between the sheath and the core yarn is activated, leading to a transition from PPR to NPR, with the magnitude of the negative value increasing monotonically

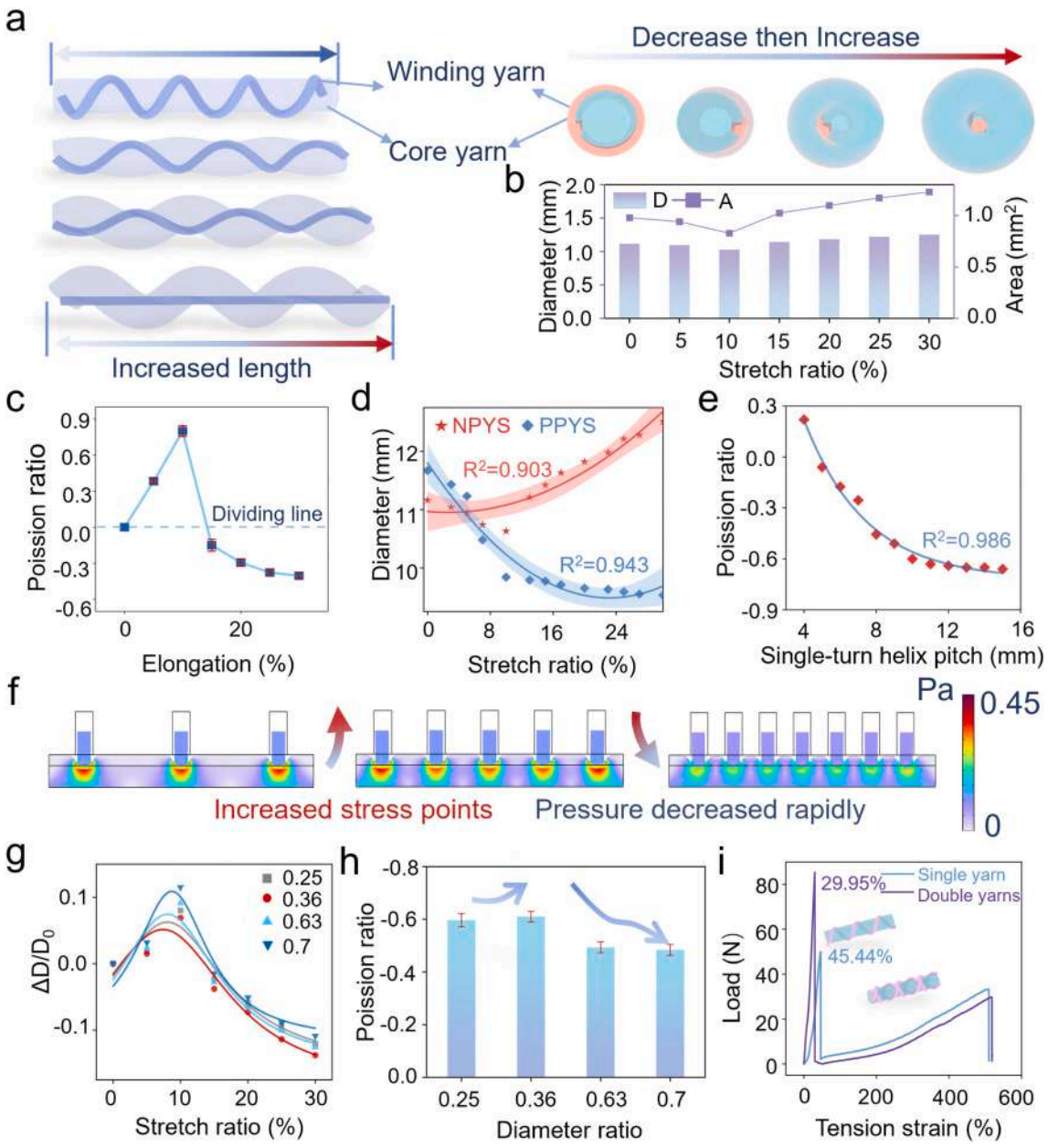


Fig. 2. NPR and mechanical properties of NPYS. a) Schematic illustration of the longitudinal and radial deformation of NPYS under tensile strains from 0% to 30%. b) Diameter and cross-sectional area as a function of tensile strain. c) Relationship between longitudinal strain and Poisson's ratio. d) Comparison of radial diameter evolution between NPR and PPR structures under identical tensile strain. e) Poisson's ratio of NPYS with different single-turn helical pitches at the same tensile strain. f) Finite element simulation of stress distribution for different single-turn helical pitches. g) Comparison of radial strain ratios of NPYS with different diameter ratios under identical tensile strain. h) Poisson's ratio as a function of diameter ratio. i) Representative stress–strain curves of the spiral and interwoven spiral structures.

with P (Note S1). Importantly, this trend does not arise from a linear amplification of radial deformation with increasing pitch, but rather from the pitch-induced regulation of deformation mechanisms and configurational transitions. Specifically, a larger pitch corresponds to a higher initial helix angle, which effectively weakens the interfacial contact constraint between the sheath and core yarn during axial stretching. This facilitates earlier sheath–core disengagement at lower axial strains. Once the critical deconstruction strain is exceeded (Note S1), the structure evolves from a constrained coupled deformation mode to one dominated by spiral unwinding and interfacial sliding. This transition substantially enhances radial expansion efficiency, thereby rapidly amplifying the NPR effect. Collectively, these results demonstrate that the single-turn helical pitch governs both the initiation and evolution of the NPR behavior by lowering the deconstruction threshold and strengthening post-deconstruction radial expansion.

Based on the above analysis, a larger pitch (P) corresponds to a smaller Poisson's ratio and a more pronounced tensile-induced deformation. However, whether this geometric advantage directly translates into enhanced electromechanical effect coupling within the piezoelectric layer remains to be clarified. To address this question, P was divided into three representative intervals, and finite element simulations were performed using COMSOL to evaluate the influence of single-turn helical pitch on the piezoelectric response. Specifically, the pressure distribution and magnitude transmitted from the functional layer to the piezoelectric layer were analyzed across different P regimes. As shown in Fig. 2f, when $P > 11.62$ mm, the functional layer exhibits efficient pressure transmission to the piezoelectric layer. For intermediate pitches (P ∈ 8.24–11.62 mm), although the pressure magnitude remains high,

the number of stress contact points between the functional and piezoelectric layers increases, leading to a partial enhancement of the piezoelectric response. In contrast, further reduction of P (P ∈ 4.86–8.24 mm) results in diminished contact pressure, thereby weakening the piezoelectric performance. These results indicate that the influence of P on piezoelectric response is inherently non-linear. Notably, optimal stress transfer from the functional layer to the piezoelectric layer is achieved within the intermediate pitch range (P ∈ 8.24–11.62 mm). This result further confirms that the negative Poisson's ratio is not linearly correlated with the piezoelectric output performance of the device.

In addition to the helical pitch, the diameter ratio between the sheath yarn and the core yarn (sheath/core) also influences the Poisson's ratio of the wound structure. To systematically tune this parameter, core yarns with different effective diameters were fabricated by bundling sheath yarns of identical diameter into single-, double-, triple-, and quadruple-strand configurations. The evolution of Poisson's ratio under these four diameter ratios was then investigated. As shown in Fig. 2g and h, the normalized diameter change ($\Delta D/D_0$) exhibits a nonmonotonic trend, first decreasing and then increasing with increasing diameter ratio. Correspondingly, the Poisson's ratio initially decreases and subsequently increases, reaching the most pronounced negative value at $\lambda = 0.36$. To elucidate the underlying mechanism, a numerical model based on the geometric deformation of the NPR structure was established (Note S2). To ensure analytical tractability, several physically reasonable assumptions were adopted: (i) the sheath yarn, regarded as an inelastic component, is effectively inextensible during deformation, such that its helical path length remains constant; (ii) no significant interfacial slip occurs between the sheath yarn and the core yarn; and (iii) the structural deformation considered in this model is dominated by geometric reconstruction rather than intrinsic material stretching. Based on these assumptions, the governing numerical model describing the geometric deformation is derived as follows:

$$\nu(\lambda) = -\left(\sqrt{p_0^2\left[(1+\varepsilon_y)^2-1\right]\Big/\pi^2 D_0^2 - 1} - 1\right)\Big/\varepsilon_y \quad (D_0 = D_a(1+\alpha\lambda)) \tag{2-4}$$

In this expression, $\nu(\lambda)$ denotes the Poisson's ratio, where λ represents the diameter ratio between the sheath yarn and the core yarn. P_0 is the initial helix pitch, ε_y is the applied axial strain, and D_0 denotes the initial equivalent structural diameter. α is a structural correction coefficient that quantifies the effective radial contribution of the wound yarn. This coefficient depends on factors including winding tightness, interfacial contact conditions, and fabrication parameters.

Based on the proposed model, an increase in the diameter ratio λ leads to a larger initial structural equivalent diameter D_0, which in turn results in an increase in Poisson's ratio. Both experimental observations.

and theoretical analysis reveal a non-monotonic dependence of the ν on λ. At low λ values, increasing the diameter of the wound yarn enhances structural compliance and facilitates radial geometric reconstruction during tensile deformation. This promotes the NPR effect. However, when λ exceeds a critical value, the initial equivalent diameter D_0 increases markedly, which suppresses relative radial deformation under axial loading. As a consequence, the conversion of axial strain into radial expansion becomes less efficient, leading to a weakened NPR effect and an increase in Poisson's ratio (Fig. S7). These results are in good agreement with the predictions of the geometry–elasticity coupling model. The tensile behaviors of the spiral and interwoven spiral structures are presented in Fig. 2i. The first fracture occurs at strains of 45.44% and 29.95% for the spiral and interwoven spiral structures, respectively, corresponding to the failure of the non-elastic sheath–core component. This indicates that the NPYS can operate stably within this deformation range. A second failure is observed at much higher strains due to rupture of the elastic yarn core, with failure strains of 509% for the spiral structure and 517% for the interwoven spiral structure.

2.3. Electrical characteristics of NPYS

As shown in Fig. S8, the XRD pattern exhibits a strong and sharp diffraction peak at $2\theta \approx 20.9°$, which is assigned to the (110/200) planes of the β phase in PVDF-TrFE [46,47]. The FTIR spectrum shows a pronounced β-phase characteristic absorption at 843 cm^{-1}. In addition, absorption bands associated with CF_2 stretching and CH_2 vibrations at 1243 cm^{-1} and 1285 cm^{-1} are prominent [48,49], whereas α-phase-related peaks are relatively weak, indicating a high β-phase content. Raman spectroscopy further confirms the formation of the β phase, showing a strong characteristic peak at 842 cm^{-1}, along with secondary peaks at 510 cm^{-1} and 1432 cm^{-1}, all of which are consistent with the ferroelectric β-phase configuration of PVDF-TrFE [50,51]. These complementary characterizations collectively demonstrate that the electrospinning process effectively induces an all-trans molecular conformation, resulting in a PVDF-TrFE electrospun film with high β-phase content and enhanced piezoelectric properties. Fig. S9 further reveals a high degree of fiber orientation in the PVDF-TrFE electrospun film.

Next, the open-circuit voltage (V_{oc}) and short-circuit current (I_{sc}) of spiral and interwoven spiral NPYS were investigated under different tensile strain ratios (Figs. 3a, b and S10). Within the strain range of 10–30%, both V_{oc} and I_{sc} exhibit a pronounced increase with increasing strain. The maximum V_{oc} reaches 5.10 V, while I_{sc} attains 64.58 nA. This enhancement is primarily attributed to the NPR effect induced by tensile loading. Specifically, under axial loading, the helical NPR yarn scaffold undergoes geometry-mediated reconfiguration, where helix rotation and radial expansion redistribute the applied axial deformation into coupled axial, radial, and interfacial shear stress components. This strain redistribution promotes more effective stress transfer to the PVDF-TrFE layer and enhances electromechanical coupling. To exclude triboelectric interference, forward and reverse connection tests were performed [52–53]. As shown in Fig. S11 a, the triboelectric effect was investigated by reversing the electrode polarity under identical mechanical loading, clamping, and environmental conditions. Figs. S11 b and c show that the output signals exhibit opposite polarities but comparable amplitudes under these conditions, confirming their piezoelectric origin. Fig. 3c compares the piezoelectric outputs of NPYS and PPYS at a relatively low tensile strain of 10% under an identical response time, revealing that the latter produces a nearly negligible signal. This result highlights the critical role of the NPR structure. Consistently, Fig. 3d compares V_{oc} and I_{sc} under identical strain ratios, demonstrating the superior tensile sensitivity of NPYS. Notably, at 30% tensile strain, the V_{oc} of NPYS is 42-fold higher than that of PPYS. Furthermore, to ensure a rigorous experimental comparison, the NPYS and PPYS in Fig. 3c and d were fabricated using the same PA sheath yarn, TPU elastic core yarn, and identical PVDF-TrFE piezoelectric film. This remarkable enhancement originates from the ability of the NPR architecture to regulate deformation pathways during stretching. Unlike the PPR structure, which undergoes axial elongation and radial contraction, resulting in a predominantly axial stress-transfer pathway, the helical NPR structure undergoes coupled axial extension and radial expansion., thereby introducing additional radial deformation and interfacial shear components. These geometry-induced stress-transfer pathways promote more effective deformation of the PVDF-TrFE layer and strengthen electromechanical coupling, resulting in significantly enhanced piezoelectric output under large-deformation conditions.

To further elucidate the piezoelectric mechanism, finite element simulations were conducted using COMSOL to analyze stress evolution and potential distribution in the piezoelectric layer before and after stretching. As shown in Fig. 3e, in the initial state, the piezoelectric layer is subjected to prestress from the encapsulation layer, enabling efficient stress transfer during subsequent deformation. At the same time, no apparent potential difference is observed. Upon tensile loading, the applied stress is transmitted to the piezoelectric layer through multiple stress-transfer sites, inducing effective compression of PVDF-TrFE and

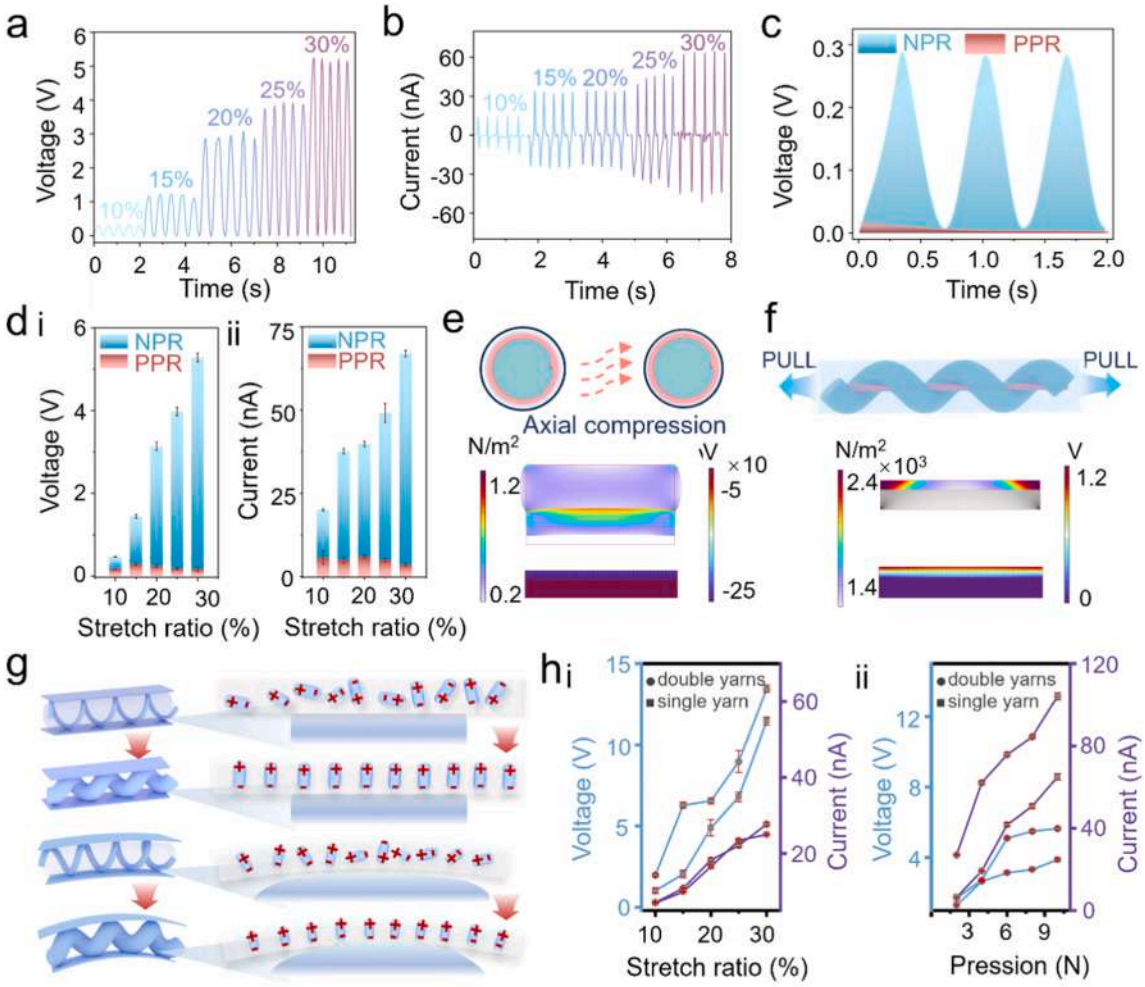


Fig. 3. Piezoelectric properties and mechanisms of NPYS. a) V_{oc} of interwoven NPYS under tensile strains from 10% to 30%. b) I_{sc} of interwoven NPYS under tensile strains from 10% to 30%. c) V_{oc} comparison between piezoelectric sensors with NPR and PPR. d) Comparison of V_{oc}(i) and I_{sc}(ii) of NPYS and PPYS under different tensile strains. e) Simulated prestress induced by the encapsulation layer on the piezoelectric layer of NPYS. f) Simulated potential distribution in the piezoelectric layer of NPYS under tensile loading. g) Schematic illustration of the piezoelectric mechanism of NPYS. h) V_{oc} and I_{sc} of NPYS and interwoven NPYS under different tensile loads (i) and compressive loads (ii).

strong electromechanical effect coupling, thereby generating a substantial potential difference across the layer (Fig. 3f). These results collectively demonstrate that the piezoelectric response of NPYS originates from the NPR effect.

Fig. 3a and b demonstrates the electromechanical performance of NPYS under uniaxial tensile loading. To further evaluate its anisotropic sensing capability, the response under vertical compressive loading was investigated. As shown in Figs. S12 and S13, compared with a PVDF-TrFE film of the same area, NPYS exhibits higher output voltage and current, together with excellent stability under cyclic compression. Under transverse compression, the cylindrical yarn mainly undergoes radial deformation, which efficiently transfers normal pressure to the PVDF-TrFE layer and enhances local stress concentration. The stable electrical responses under both axial tension and vertical compression indicate that NPYS maintains robust electromechanical coupling under distinct stress states, namely axial strain and normal pressure. In addition, bending deformation intrinsically arises from the superposition of in-plane tensile and compressive strains, which generates a tensile–compressive strain gradient across the thickness of the piezoelectric layer and consequently induces asymmetric stress distribution and dipole polarization. Therefore, the demonstrated stability under pure tensile and compressive loading supports reliable electrical output under bending deformation. The anisotropic sensing capability of NPYS fundamentally originates from its rational structural design.

Fig. 3g illustrates the dynamic evolution of dipole orientation and deflection behavior within the piezoelectric layer under different deformation modes. As shown in Fig. 3h, both helical and interwoven-helical NPYS exhibit monotonic increases in output voltage and current with increasing strain and applied pressure, indicating quantitatively stable anisotropic sensing performance. Moreover, the interwoven helical NPYS shows stronger responses than the helical structure in both modes, demonstrating that the synergistic structural design not only amplifies signal intensity but also enhances the reliability of anisotropic sensing across different mechanical dimensions. Figs. S14 and S15 characterize the response time, recovery time and cyclic stability of NPYS. After undergoing 10,000 cycle tests, the NPYS maintained a fundamentally stable output voltage, demonstrating the device's outstanding stability.

2.4. Anisotropic applications of NPR yarn-based sensors for rehabilitation training systems

In practical rehabilitation training, different movement patterns correspond to distinct mechanical deformation modes. Joint flexion/extension and muscle traction are mainly associated with axial stretching, whereas standing, stepping, and human–device interactions are dominated by vertical compression. If a single flexible piezoelectric device can discriminate and respond to these representative mechanical

states, continuous and quantitative monitoring of rehabilitation processes can be achieved without increasing system complexity, thereby providing reliable data support for rehabilitation monitoring systems [48]. As a proof of concept, the sensing performance of the NPYS was systematically evaluated under axial stretching, vertical compression, and bending deformations to assess its applicability in rehabilitation training. When integrated into elastic bands (Fig. 4b), NPYS enabled real-time monitoring of axial stretching. Distinct voltage outputs were obtained at different strain levels in resistance bands, with the output amplitude increasing monotonically with applied strain (Fig. 4a). A complete stretching–releasing cycle generated a single electrical signal cycle, demonstrating the capability of NPYS to continuously capture stretching motions (Fig. 4c). For vertical compression and bending modes, NPYS was embedded in insoles or mounted on human joints, including fingers, knees, and ankles. Electrical signals generated during different training movements.

exhibited pronounced differences in both amplitude and frequency, enabling effective discrimination of movement types and motion states

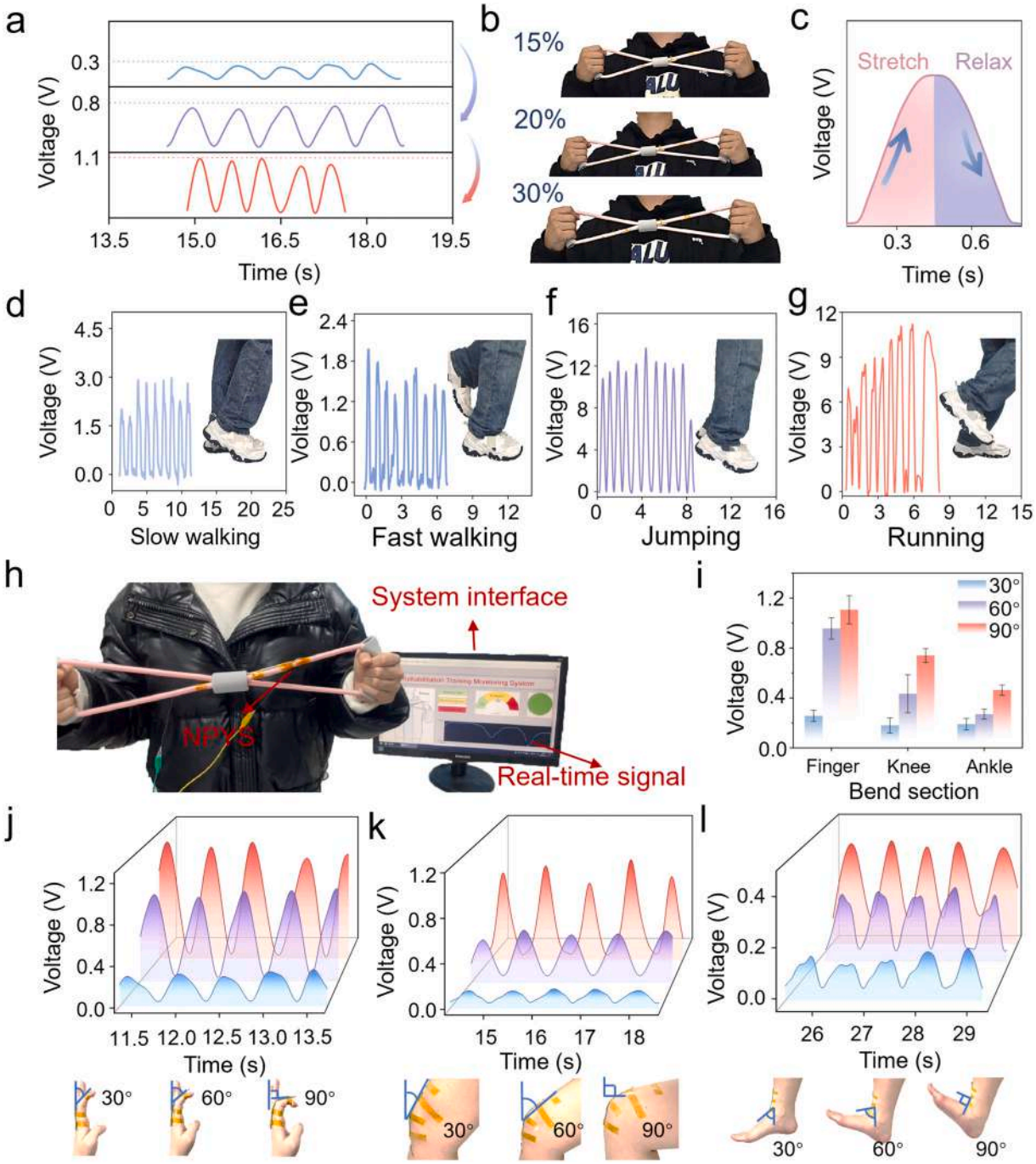


Fig. 4. Anisotropic application demonstration and rehabilitation training monitoring system. a) V_{oc} of NPYS under elastic-band stretching with strain ranging from 15% to 30%. b) Photographs of NPYS integrated into elastic bands at stretching strains from 15% to 30%. c) Representative electrical signal corresponding to one complete stretching–releasing cycle. d-g) Electrical signals and corresponding photographs of NPYS integrated into the shoe insoles during slow walking, fast walking, jumping, and running, respectively. h) Photograph of rehabilitation training monitoring using NPYS. i) Electrical responses of NPYS attached to the finger, knee, and ankle joints under bending angles from 30° to 90°. j-l) Electrical signals and corresponding photographs of NPYS attached to finger, knee, and ankle joints at different bending angles.

(Fig. 4d–g, j–l). Notably, distinct signal responses were observed at bending angles of 30°, 60°, and 90°, with output voltage showing a monotonic increase with bending angle (Fig. 4i). Among the tested sites, finger joints exhibited the highest bending sensitivity. These results demonstrate that NPYS can identify complex rehabilitation movements through combined analysis of signal amplitude and frequency, providing a reliable sensing platform for rehabilitation training monitoring.

Based on these results, a rehabilitation training monitoring system was developed [24]. Fig. 4h presents a representative photograph of a subject performing stretching rehabilitation using elastic bands integrated with NPYS. The supplementary materials include videos demonstrating the rehabilitation training monitoring system, specifically its applications in stretch force measurement and plantar pressure sensing with real-time feedback (Movies S1 and S2). The system incorporates NPYS as the sensing unit to acquire mechanical signals generated during training in real time. The collected signals are processed through a signal modulation and analysis module to extract the training force as a key quantitative parameter. Real-time signals are continuously compared with predefined safety thresholds to enable dynamic assessment of training status. When the measured parameters exceed the threshold range, a control and feedback module is automatically activated to trigger warning signals and guide users to adjust training intensity until the signals return to a safe range. Through this closed-loop sensing–feedback strategy, the system achieves real-time regulation and quantitative evaluation of rehabilitation training while maintaining a structurally simple configuration. The detailed signal-processing and feedback workflow is provided in Note S3. Overall, these demonstrations highlight the effectiveness of NPYS for anisotropic monitoring of complex human motion. The proposed system offers a reliable approach for quantifying training intensity and reducing potential risks in rehabilitation training.

3. Conclusion

In this work, an NPYS based on a helical architecture was developed to overcome the limited anisotropic sensing capability of conventional flexible piezoelectric sensors. The TPU/PA helical yarn provides intrinsic NPR behavior and high stretchability, while the PVDF-TrFE electrospun fiber film contributes robust piezoelectric performance. Owing to the synergistic integration of structure and material, NPYS exhibits excellent mechanical compliance and can achieve anisotropic sensing capabilities for axial tension, normal compression, and bending gradients. Furthermore, NPYS is inherently compatible with textile integration, highlighting its potential for flexible electronic textiles. As a proof of concept, NPYS demonstrates reliable monitoring of diverse physiological signals on complex curved body surfaces and enables real-time tracking and feedback when incorporated into a rehabilitation training monitoring system. This work establishes a versatile strategy for anisotropic sensing using flexible piezoelectric yarns and underscores their promise in wearable electronics, electronic textiles, and human–machine interaction.

4. Experimental section

4.1. Materials

Poly(vinylidene fluoride–trifluoroethylene) (PVDF-TrFE, 80:20) powder was purchased from Beijing Guangtai Runbo Technology Co., Ltd. *N*,*N*-dimethylformamide (DMF, 99.9%) and acetone (AC, 99.9%) were obtained from Aladdin Reagent Co., Ltd. All chemical reagents were used as received without further purification. Polyurethane elastic yarn (PU, diameter 1 mm) and polyamide yarn (PA, diameter 0.27 mm) were supplied by Dongguan Yuechao Thread Co., Ltd. Transparent poly (vinyl chloride) (PVC) tubing with a diameter of 2.5 mm was purchased from Wenzhou Yingbo Electric Co., Ltd.

4.2. Preparation of the PVDF-TrFE nanofibers

A PVDF-TrFE electrospinning solution was prepared by dissolving 0.5 g of PVDF-TrFE (80:20) in a mixed solvent of N·*N*-dimethylformamide and acetone (*v*/v = 1:1, total volume 5 mL). The solution was magnetically stirred at room temperature for 12 h to obtain a homogeneous solution, followed by degassing under vacuum to remove trapped air bubbles. The resulting solution was loaded into a 10 mL syringe for electrospinning. Electrospinning was carried out at an applied voltage of 15–17 kV with a flow rate of 1.0 mL h^{-1}. The distance between the needle tip and the rotating collector was fixed at 13 cm, and the collector rotation speed was set to 1000 rpm. After electrospinning, the collected PVDF-TrFE nanofiber films were annealed at 100 °C for 3 h.

4.3. Preparation of NPYS

The PVDF-TrFE nanofiber film (98 mm × 4 mm) was first encapsulated. Silver electrodes were deposited on both sides of the film by magnetron sputtering under an argon atmosphere. Copper wires were electrically connected using carbon cloth, and the assembly was encapsulated with a flexible, high-temperature-resistant polyimide (PI) film. NPR yarns were fabricated by helically winding polyamide (PA) yarn around a polyurethane (TPU) core yarn with a defined helix length (5–15 mm) and winding angle, followed by bonding of the two yarns ends. The encapsulated PVDF-TrFE film was then helically wrapped around the NPR yarn and enclosed within a transparent poly(vinyl chloride) (PVC) tube, yielding the complete NPYS.

4.4. Finite element analysis

Finite element analysis (FEA) was conducted to evaluate the piezoelectric response modes of the designed device. The model geometry was defined according to the actual device dimensions. To reduce computational complexity, the electrospun PVDF-TrFE film was approximated as a homogeneous continuum with a Young's modulus of 800 kPa and a Poisson's ratio of 0.35. The present finite-element model was primarily developed to elucidate the stress-transfer behavior of the NPR structure during tensile deformation and its effect on the piezoelectric layer. Accordingly, piezoelectric multiphysics coupling and interfacial contact evolution were not explicitly considered in the current model. Therefore, the simulation results are intended to clarify the electromechanical coupling mechanism and its variation trend.

4.5. Materials characteristics and measurement of electric performance

The morphology of the PVDF-TrFE electrospun films was characterized by field-emission scanning electron microscopy (FESEM, JSM-7800F, JEOL) operated at 15 kV, coupled with energy-dispersive X-ray spectroscopy (EDS). The crystalline structure was analyzed using X-ray diffraction (XRD, Empyrean, PANalytical), while Fourier-transform infrared spectroscopy (FTIR, Nicolet iS50, ATR mode) and Raman spectroscopy (RM2000, 514 nm excitation) were employed to investigate the phase composition and molecular conformation further. The pressure sensing performance was evaluated by applying controlled compressive loads using a linear motor (LinMot H01–23 × 86/160) integrated with a force sensor (M7–50, Mark-10), allowing real-time force monitoring. Tensile sensing performance was assessed using a universal testing machine (UTM, Shanghai Songdun Instrument Manufacturing Co., Ltd.) under controlled tensile loading conditions. The corresponding voltage and current outputs were recorded in real time using a Keithley 6517 electrometer.

CRediT authorship contribution statement

Guicen Liu: Writing – original draft, Methodology, Formal analysis, Conceptualization. **Long Jin:** Supervision, Resources, Funding

acquisition. **Yong Ao:** Investigation, Formal analysis. **Boling Lan:** Project administration, Methodology. **Tianpei Xu:** Validation, Software. **Shenglong Wang:** Project administration, Methodology. **Tingting Zhou:** Visualization, Supervision. **Zihan Wang:** Visualization. **Wei Zhao:** Supervision. **Zhiyuan Gao:** Visualization. **Weili Deng:** Supervision, Project administration. **Weiqing Yang:** Supervision, Funding acquisition.

Declaration of competing interest

The authors declare no competing interests.

Acknowledgments

The National Natural Science Foundation of China (No. 52303328), the Postdoctoral Innovation Talents Support Program (No. BX20220257). The authors also want to thank the full support from the Analysis and Testing Center of Southwest Jiaotong University.

Appendix A. Supplementary data

Supplementary data to this article can be found online at https://doi.org/10.1016/j.cej.2026.181531.

Data availability

Data will be made available on request.

References

[1] Y. Shi, Y. Guan, M. Liu, X. Kang, Y. Tian, W. Deng, P. Yu, C. Ning, L. Zhou, R. Fu, G. Tan, Tough, antifreezing, and piezoelectric organohydrogel as a flexible wearable sensor for human–machine interaction, ACS Nano 18 (4) (2024) 3720–3732, https://doi.org/10.1021/acsnano.3c11578.

[2] S. Song, M. Zhang, X. Gong, S. Shi, J. Fang, X. Wang, Advances in wearable sensors for health management from advanced materials, Adv. Funct. Mater. 36 (11) (2026) e18767, https://doi.org/10.1002/adfm.202518767.

[3] T.Q. Trung, N.-E. Lee, Flexible and stretchable physical sensor integrated platforms for wearable human-activity Monitoringand personal healthcare, Adv. Funct. Mater. 28 (22) (2016) 4338–4372, https://doi.org/10.1002/adma.201504244.

[4] X. Chen, C. Wang, W. Wei, Y. Liu, S.S. Ge, L. Zhou, H. Kong, Flexible and sensitive pressure sensor with enhanced breathability for advanced wearable health monitoring, NPJ Flexible Electron. 9 (1) (2025) 101, https://doi.org/10.1038/s41528-025-00469-6.

[5] S. Sharma, G.B. Pradhan, S. Jeong, S. Zhang, H. Song, J.Y. Park, Stretchable and all-directional strain-insensitive electronic glove for robotic skins and human–machine interfacing, ACS Nano 17 (9) (2023) 8355–8366, https://doi.org/10.1021/acsnano.2c12784.

[6] J. He, R. Zhou, Y. Zhang, W. Gao, T. Chen, W. Mai, C. Pan, Strain-insensitive self-powered tactile sensor arrays based on intrinsically stretchable and patternable ultrathin conformal wrinkled graphene-elastomer composite, Adv. Funct. Mater. 32 (10) (2022) 2107281, https://doi.org/10.1002/adfm.202107281.

[7] J. Qu, G. Cui, Z. Li, S. Fang, X. Zhang, A. Liu, M. Han, H. Liu, X. Wang, X. Wang, Advanced flexible sensing technologies for soft robots, Adv. Funct. Mater. 34 (29) (2024) 2401311, https://doi.org/10.1002/adfm.202401311.

[8] R. Baines, F. Zuliani, N. Chennoufi, S. Joshi, R. Kramer-Bottiglio, J. Paik, Multi-modal deformation and temperature sensing for context-sensitive machines, Nat. Commun. 14 (1) (2023) 7499, https://doi.org/10.1038/s41467-023-42655-y.

[9] A. Leber, C. Dong, R. Chandran, T. Das Gupta, N. Bartolomei, F. Sorin, Soft and stretchable liquid metal transmission lines as distributed probes of multimodal deformations, Nat. Electron. 3 (6) (2020) 316–326, https://doi.org/10.1038/s41928-020-0415-y.

[10] P. Li, Y. Feng, C. Ding, R. Zhong, W. Yan, J. Song, Z. Hong, B. Hu, J. Tan, J. Sun, X. Song, Magnetointeractive Cr2Te3-coated liquid metal droplets for flexible memory arrays and wearable sensors, Adv. Mater. (Weinheim, Ger.) 37 (13) (2025) 2414519, https://doi.org/10.1002/adma.202414519.

[11] Y. Zheng, Y. Li, Y. Zhao, X. Lin, S. Luo, Y. Wang, L. Li, C. Teng, X. Wang, G. Xue, D. Zhou, Ultrathin and highly breathable electronic tattoo for sensing multiple signals imperceptibly on the skin, Nano Energy 107 (2023) 108092, https://doi.org/10.1016/j.nanoen.2022.108092.

[12] Y. Bai, Y. Zhou, X. Wu, M. Yin, L. Yin, S. Qu, F. Zhang, K. Li, Y. Huang, Flexible strain sensors with ultra-high sensitivity and wide range enabled by crack-modulated electrical pathways, Nano-Micro Lett. 17 (1) (2024) 64, https://doi.org/10.1007/s40820-024-01571-6.

[13] Y. Wang, Y. Yue, F. Cheng, Y. Cheng, B. Ge, N. Liu, Y. Gao, Ti3C2Tx MXene-based flexible Piezoresistive physical sensors, ACS Nano 16 (2) (2022) 1734–1758, https://doi.org/10.1021/acsnano.1c09925.

[14] L. Tian, F.-L. Gao, Y.-X. Li, Z.-Y. Yang, X. Xu, Z.-Z. Yu, J. Shang, R.-W. Li, X. Li, High-performance bimodal temperature/pressure tactile sensor based on lamellar CNT/MXene/cellulose nanofibers aerogel with enhanced multifunctionality, Adv. Funct. Mater. 35 (17) (2025) 2418988, https://doi.org/10.1002/adfm.202418988.

[15] X. Zhou, W. Cao, Flexible and stretchable carbon-based sensors and actuators for soft robots, Nanomaterials (Basel, Switzerland) 13 (2) (2023) 316.

[16] X. Yang, H. Liu, T. Pan, B. Li, J. Chu, Highly foldable and leakage-free electrodes enabled by ultrathin liquid metal micromeshes, NPJ Flexible Electron. 10 (1) (2025) 10, https://doi.org/10.1038/s41528-025-00510-8.

[17] S. Liu, W. Zhang, J. He, Y. Lu, Q. Wu, M. Xing, Fabrication techniques and sensing mechanisms of textile-based strain sensors: from spatial 1D and 2D perspectives, Adv. Fiber Mater. 6 (1) (2024) 36–67, https://doi.org/10.1007/s42765-023-00338-9.

[18] M. Song, Q. Liu, X. Xu, B. Wang, Y. Lu, L. Yang, X. Liu, Y. Wang, M. Li, D. Wang, A fabric-based multimodal flexible tactile sensor with precise sensing and discrimination capabilities for pressure-proximity-magnetic field signals, Adv. Funct. Mater. 35 (19) (2025) 2420445, https://doi.org/10.1002/adfm.202420445.

[19] Q. Yu, J. Pan, Z. Jiang, Z. Guo, J. Jiang, Stretchable multimodal textile sensor based on core-sheath CB/PDMS/MXene sensing yarn for efficiently distinguishing mechanical stimulus, Chem. Eng. J. 493 (2024) 152462, https://doi.org/10.1016/j.cej.2024.152462.

[20] S. Wang, W. Deng, H. Huang, Z. Yan, Y. Wang, T. Zhou, Y. Ao, Z. Wang, J. Zhang, G. Tian, B. Lan, Y. Sun, T. Xu, T. Yang, L. Huang, L. Jin, J. Lu, W. Yang, Strain-invariant omnidirectional stretchable MXetronics, Nat. Commun. 17 (1) (2026) 2471, https://doi.org/10.1038/s41467-026-68925-z.

[21] Y. Sun, G. Tian, W. Deng, W. Yang, Ionic hydrogel sensors toward next-gen personalized healthcare, Adv. Mater. 38 (3) (2026) e09122, https://doi.org/10.1002/adma.202509122.

[22] Y. Ao, L. Jin, S. Wang, B. Lan, G. Tian, T. Xu, L. Huang, Z. Wang, Y. Sun, T. Yang, W. Deng, F. Yang, W. Yang, Dual structure reinforces interfacial polarized MXene/PVDF-TrFE piezoelectric nanocomposite for pressure monitoring, Nano-Micro Lett. 17 (1) (2025) 320, https://doi.org/10.1007/s40820-025-01839-5.

[23] Y. Sun, G. Tian, T. Yang, S. Wang, B. Lan, X. Li, T. Xu, L. Jin, W. Deng, W. Yang, Crosslinking-modulated hydrogel piezoionic sensor for pattern security authentication in human-machine interfaces, Adv. Funct. Mater. 35 (19) (2025) 2420187, https://doi.org/10.1002/adfm.202420187.

[24] G. Tian, W. Deng, T. Yang, J. Zhang, T. Xu, D. Xiong, B. Lan, S. Wang, Y. Sun, Y. Ao, L. Huang, Y. Liu, X. Li, L. Jin, W. Yang, Hierarchical piezoelectric composites for noninvasive continuous cardiovascular monitoring, Adv. Mater. (Weinheim, Ger.) 36 (26) (2024) 2313612, https://doi.org/10.1002/adma.202313612.

[25] L. Xing, L. Li, Y. Liu, J. Ren, G. Guo, Y. Chen, Y. Zheng, B. Sun, Highly stretchable GR/TPU strain sensor based on one-step electrospun fibrous yarns for wearable devices, J. Mater. Chem. A 12 (18) (2024) 10905–10912, https://doi.org/10.1039/D4TA00176A.

[26] X. Qu, Y. Wu, P. Ji, B. Wang, Q. Liang, Z. Han, J. Li, Z. Wu, S. Chen, G. Zhang, H. Wang, Crack-based core-sheath fiber strain sensors with an ultralow detection limit and an ultrawide working range, ACS Appl. Mater. Interfaces 14 (25) (2022) 29167–29175, https://doi.org/10.1021/acsami.2c04559.

[27] Q. Chen, Y. Xiong, Y. Wang, J. Wang, S. Zhou, G. Sun, H. Hu, Y. Du, J. Kong, Z. Liu, N. Meng, Y. Liao, Architecturally partitioned core-sheath woven fabric for integrated electromagnetic wave absorption and self-powered non-contact sensing, Adv. Funct. Mater. 36 (15) (2026) e18158, https://doi.org/10.1002/adfm.202518158.

[28] H. Lin, H. Wang, Y. Yang, Y. Zhang, L. Li, Y. Zhao, W. Zhang, Smart fabrics with liquid metal reinforced PU/CNT/MXene multilayer structures for constructing multifunctional sensors and wearable electronics, J. Mater. Chem. A 12 (44) (2024) 30872–30884, https://doi.org/10.1039/D4TA05266H.

[29] H. Jiang, R. Zhang, K. Liu, Y. Luo, Z. Peng, S. Ye, Y. Qin, X. Wu, C. Gao, Y. Liu, D. Xu, W. Xu, Wet-adaptive strain sensor based on hierarchical core-sheath yarns for underwater motion monitoring and energy harvesting, Nano Energy 132 (2024) 110407, https://doi.org/10.1016/j.nanoen.2024.110407.

[30] X. Li, K.H. Koh, M. Farhan, K.W.C. Lai, An ultraflexible polyurethane yarn-based wearable strain sensor with a polydimethylsiloxane infiltrated multilayer sheath for smart textiles, Nanoscale 12 (6) (2020) 4110–4118, https://doi.org/10.1039/C9NR09306K.

[31] Z.F. Liu, S. Fang, F.A. Moura, J.N. Ding, N. Jiang, J. Di, M. Zhang, X. Lepró, D. S. Galvão, C.S. Haines, N.Y. Yuan, S.G. Yin, D.W. Lee, R. Wang, H.Y. Wang, W. Lv, C. Dong, R.C. Zhang, M.J. Chen, Q. Yin, Y.T. Chong, R. Zhang, X. Wang, M.D. Lima, R. Ovalle-Robles, D. Qian, H. Lu, R.H. Baughman, Hierarchically buckled sheath-core fibers for superelastic electronics, sensors, and muscles, Sci. Sports 349 (6246) (2015) 400–404, https://doi.org/10.1126/science.aaa7952.

[32] X. Zhou, K. Parida, J. Chen, J. Xiong, Z. Zhou, F. Jiang, Y. Xin, S. Magdassi, P. S. Lee, 3D printed auxetic structure-assisted piezoelectric energy harvesting and sensing, Adv. Energy Mater. 13 (34) (2023) 2301159, https://doi.org/10.1002/aenm.202301159.

[33] M. Razbin, R. Bagherzadeh, M. Asadnia, S. Wu, Recent advances in wearable electromechanical sensors based on Auxetic textiles, Adv. Funct. Mater. 34 (49) (2024) 2409242, https://doi.org/10.1002/adfm.202409242.

[34] S. Zhao, Y. Zhang, G. Li, Y. Zhou, M. Xia, A.T. Hoang, Y. Gao, D. Cao, G. Li, Y. Li, Y. Lai, J.-H. Ahn, Mussel-inspired highly sensitive, stretchable, and self-healable yarns enabled by dual conductive pathways and encapsulation for wearable electronics, Adv. Funct. Mater. 35 (7) (2025) 2412461, https://doi.org/10.1002/adfm.202412461.

[35] Y. Luo, L. Zhao, G. Luo, L. Dong, Y. Xia, M. Li, Z. Li, K. Wang, R. Maeda, Z. Jiang, Highly sensitive piezoresistive and thermally responsive fibrous networks from the in situ growth of PEDOT on MWCNT-decorated electrospun PU fibers for pressure

and temperature sensing, Microsyst. Nanoeng. 9 (1) (2023) 113, https://doi.org/10.1038/s41378-023-00593-1.
[36] Z. Feng, Q. He, X. Wang, J. Qiu, H. Wu, Y. Lin, Y. Wu, J. Yang, Waterproof Iontronic yarn for highly sensitive biomechanical strain monitoring in wearable electronics, Adv. Fiber Mater. 6 (3) (2024) 925–935, https://doi.org/10.1007/s42765-024-00381-0.
[37] R. Wu, S. Seo, L. Ma, J. Bae, T. Kim, Full-Fiber Auxetic-interlaced yarn sensor for sign-language translation glove assisted by artificial neural network, Nano-Micro Lett. 14 (1) (2022) 139, https://doi.org/10.1007/s40820-022-00887-5.
[38] T.J. Cuthbert, B.C. Hannigan, P. Roberjot, A.V. Shokurov, C. Menon, HACS: helical auxetic yarn capacitive strain sensors with sensitivity beyond the theoretical limit, Adv. Mater. (Weinheim, Ger.) 35 (10) (2023) 2209321, https://doi.org/10.1002/adma.202209321.
[39] J. Wang, S. Liu, Z. Chen, T. Shen, Y. Wang, R. Yin, H. Liu, C. Liu, C. Shen, Ultrasensitive electrospinning fibrous strain sensor with synergistic conductive network for human motion monitoring and human-computer interaction, J. Mater. Sci. Technol. 213 (2025) 213–222, https://doi.org/10.1016/j.jmst.2024.07.003.
[40] O. Yue, X. Wang, Y. Zhou, Z. Bai, X. Zou, L. Xie, X. Liu, Auxetic structure-assisted triboelectric nanogenerators for efficient energy collection and wearable sensing, Adv. Energy Mater. 14 (24) (2024) 2400212, https://doi.org/10.1002/aenm.202400212.
[41] S. Li, C. Liu, W. Chen, J. Huang, L. Gan, Negative Poisson's ratio in cellulose nanocrystal aerogels for enhanced sports piezoelectric sensing, Adv. Funct. Mater. 35 (29) (2025) 2418425, https://doi.org/10.1002/adfm.202418425.
[42] L. Chen, C. Chen, L. Jin, H. Guo, A.C. Wang, F. Ning, Q. Xu, Z. Du, F. Wang, Z. L. Wang, Stretchable negative Poisson's ratio yarn for triboelectric nanogenerator for environmental energy harvesting and self-powered sensor, Energy Environ. Sci. 14 (2) (2021) 955–964, https://doi.org/10.1039/D0EE02777D.
[43] X. Zhang, Q. Sun, X. Liang, P. Gu, Z. Hu, X. Yang, M. Liu, Z. Sun, J. Huang, G. Wu, G. Zu, Stretchable and negative-Poisson-ratio porous metamaterials, Nat. Commun. 15 (1) (2024) 392, https://doi.org/10.1038/s41467-024-44707-3.
[44] M.-M. Yang, T.-Y. Zhu, A.B. Renz, H.-M. Sun, S. Liu, P.M. Gammon, M. Alexe, Auxetic piezoelectric effect in heterostructures, Nat. Mater. 23 (1) (2024) 95–100, https://doi.org/10.1038/s41563-023-01736-5.
[45] X. Liu, W. Wang, X. Wang, Y. Zhou, L. Li, L. Xing, W. Zhang, O. Yue, Efficient triboelectric nanogenerators with on-demand auxetic structure achieving deformation matching in wearable devices, Nano Energy 135 (2025) 110648, https://doi.org/10.1016/j.nanoen.2025.110648.
[46] S. Yang, X. Qiao, J. Ma, Z. Yang, X. Luo, Z. Du, Recent advances in flexible sensors for neural interfaces: multimodal sensing, signal integration, and closed-loop feedback, Biosens. Bioelectron. 15 (7) (2025) 424.
[47] Y. Ao, T. Yang, G. Tian, S. Wang, T. Xu, L. Deng, J. Zhang, L. Tang, W. Deng, L. Jin, W. Yang, Tertiary orientation structures enhance the piezoelectricity of MXene/PVDF nanocomposite, Nano Res. 17 (6) (2024) 5629–5635, https://doi.org/10.1007/s12274-023-6418-7.
[48] L. Jin, Y. Ao, T. Xu, J. Zhang, Y. Zou, B. Lan, S. Wang, W. Deng, W. Yang, Confined orientation PVDF/MXene nanofibers for wearable piezoelectric nanogenerators, J. Mater. Chem. A 13 (20) (2025) 14446–14454, https://doi.org/10.1039/D4TA08879D.
[49] Z. Wang, S. Wang, B. Lan, Y. Sun, L. Huang, Y. Ao, X. Li, L. Jin, W. Yang, W. Deng, Piezotronic sensor for bimodal monitoring of Achilles tendon behavior, Nano-Micro Lett. 17 (1) (2025) 241, https://doi.org/10.1007/s40820-025-01757-6.
[50] T. Yang, H. Pan, G. Tian, B. Zhang, D. Xiong, Y. Gao, C. Yan, X. Chu, N. Chen, S. Zhong, L. Zhang, W. Deng, W. Yang, Hierarchically structured PVDF/ZnO core-shell nanofibers for self-powered physiological monitoring electronics, Nano Energy 72 (2020) 104706, https://doi.org/10.1016/j.nanoen.2020.104706.
[51] L. Jin, X. Xiao, W. Deng, A. Nashalian, D. He, V. Raveendran, C. Yan, H. Su, X. Chu, T. Yang, W. Li, W. Yang, J. Chen, Manipulating relative permittivity for high-performance wearable triboelectric Nanogenerators, Nano Lett. 20 (9) (2020) 6404–6411, https://doi.org/10.1021/acs.nanolett.0c01987.
[52] T. Zhou, S. Wang, Y. Ao, B. Lan, Y. Sun, G. Tian, T. Yang, L. Huang, L. Jin, L. Tang, W. Yang, W. Deng, High-temperature-resistance flexible piezoelectric sensor via cyclized PAN/BTO nanofibers, Nano Energy 138 (2025) 110910, https://doi.org/10.1016/j.nanoen.2025.110910.
[53]].M. Xie, Y. Bao, T. Hu, J. Wu, W. Liu, S. He, T. Zhang, S. Guo, H. Nie, Y. Lin, H. Huang, N. Meng, G. Wang, Reversible giant pyroelectricity for enhanced energy harvesting and solar-driven pyro-catalysis, Matter 9 (5) (2026), https://doi.org/10.1016/j.matt.2026.102708.